Crystalline symmetry controlled magnetic switching in epitaxial (111) $La_{0.7}Sr_{0.3}MnO_3$ thin films

I. Hallsteinsen, E. Folven, F. K. Olsen, R. V. Chopdekar (iD), M. S. Rzchowski, C. B. Eom, J. K. Grepstad, and T. Tybell (iD)

Crystalline symmetry controlled magnetic switching in epitaxial (111) La$_{0.7}$Sr$_{0.3}$MnO$_3$ thin films

I. Hallsteinsen,[1] E. Folven,[1] F. K. Olsen,[1] R. V. Chopdekar,[2]
M. S. Rzchowski,[3] C. B. Eom,[4] J. K. Grepstad,[1] and T. Tybell[1,a]

[1]*Department of Electronics and Telecommunications, Norwegian University of Science and Technology, Trondheim 7491, Norway*
[2]*Department of Chemical Engineering and Materials Science, University of California-Davis, Davis, California 95616, USA*
[3]*Department of Physics, University of Wisconsin-Madison, Madison, Wisconsin 53706, USA*
[4]*Department of Materials Science and Engineering, University of Wisconsin-Madison, Madison, Wisconsin 53706, USA*

Mixed-valence manganite thin films are attractive for spintronic devices. Crystalline orientation is a promising route to tailor switching mechanisms, as magnetization reversal depends on the magnetic anisotropy. Here, magnetic properties of (111)-oriented La$_{0.7}$Sr$_{0.3}$MnO$_3$ thin films are elucidated by correlating macroscopic and local properties. The coercive field is an order of magnitude lower than (001)-oriented La$_{0.7}$Sr$_{0.3}$MnO$_3$. Locally, a 6-fold magnetic anisotropy is observed, while macroscopically, an isotropic response is prevailing. This local coupling between the symmetry of the (111)-facet and magnetization governs the domain reversal process, demonstrating that symmetry offers a route to control magnetic properties for spintronic devices. © 2015 Author(s). All article content, except where otherwise noted, is licensed under a Creative Commons Attribution 3.0 Unported License. [http://dx.doi.org/10.1063/1.4907877]

Mixed-valence manganites have attracted considerable attention due to the demonstration of colossal magnetoresistance (CMR)[1] and a high degree of spin polarization.[2] Hence, manganites are attractive candidates for electrode materials in spintronic devices such as magnetic tunnel junctions.[3] To assess the case for implementation of these materials in spintronic devices, the physical properties of manganite thin films have been extensively studied as a function of epitaxial strain and chemical doping.[3]

La$_{0.7}$Sr$_{0.3}$MnO$_3$ is a ferromagnetic half-metal at room temperature with a Curie temperature of ~350 K for thin films.[4,5] This makes La$_{0.7}$Sr$_{0.3}$MnO$_3$ a good candidate for room-temperature magnetoresistive devices such as field sensors and magnetic memories.[6,7] The low-field magneto-resistive response in manganites relies on magnetization reversal processes,[8,9] dependent on the magnetic anisotropy of the system.[10]

In single crystals of La$_{0.7}$Sr$_{0.3}$MnO$_3$, the magnetic anisotropy originates from the rhombohedral distortion of the unit cell, and the magnetization vector lies in a (111) easy plane.[8,11] However, in thin films of (001)-oriented La$_{0.7}$Sr$_{0.3}$MnO$_3$, tensile strain confines the magnetization to be in the film plane,[12] either with biaxial anisotropy along ⟨110⟩ directions due to the orbital structure[11,13] or with uniaxial anisotropy aligned with the film step-edges. (110)-oriented thin films have an anisotropic Young's modulus, so that magnetostriction dominates over crystalline effects in defining the magnetic anisotropy.[13] In this case, the anisotropy is uniaxial along the [001] crystalline axis, with an out-of-plane contribution along the extended body diagonal in the [111]-direction.[14] Thus, the magnetic anisotropy in thin films can be tuned by step-edges, lattice strain, film thickness, and

---

[a]Email: thomas.tybell@iet.ntnu.no

substrate orientation, which open up the possibilities to tailor the magnetic reversal mechanisms for device technology.

Recently, there has been a large interest on the possibilities that (111)-oriented perovskite thin films can offer due to their non-cubic crystalline surface symmetry.[15,16] The crystallographic structure of the (111)-plane in $SrTiO_3$ is hexagonal where the in-plane low index crystallographic axes belong to $\langle 1\text{-}10 \rangle$ and $\langle 11\text{-}2 \rangle$, as shown in Figure 1. The rhombohedral unit cell of $La_{0.7}Sr_{0.3}MnO_3$ on (111)-oriented $SrTiO_3$ undergoes a trigonal distortion. The lattice mismatch is, however, the same as for (001)-oriented $SrTiO_3$ and the biaxial Young's modulus is isotropic. Hence, for (111)-oriented films on $SrTiO_3$, we expect tensile strain and in-plane magnetization, where the magnetic anisotropy is predominated by magneto-crystalline effects rather than magnetostriction.[17]

Here, we investigate how the hexagonal symmetry affects the magnetic properties of epitaxial thin films of $La_{0.7}Sr_{0.3}MnO_3$ grown on (111) $SrTiO_3$ substrates. Relying on local domain imaging during magnetization reversal, we demonstrate a magneto-crystalline coupling making the in-plane directions of [1-10] and [11-2] easy axes, and that the magnetization reversal proceeds by domains nucleating successively along these in-plane directions.

Epitaxial $La_{0.7}Sr_{0.3}MnO_3$ thin films were fabricated on (111)-oriented Nb-doped (0.05%) $SrTiO_3$ substrates by pulsed laser deposition.[18] The substrates were chosen to prevent charging during the local domain imaging and were prepared by ultrasonic agitation in deionized water at 70 °C, etched in buffered hydrofluoric acid for 45 s and annealed for 1 h at 1050 °C in an oxygen ambient. Atomic force microscopy (AFM, Veeco Nanoscope V) showed step-and-terrace substrates with step heights of 2.25 Å, corresponding to the distance between adjacent (111)-planes, terrace widths of 100 nm, which is in good accordance with the miscut angle of 0.1°, and films of all thicknesses replicated the surface topography of the substrates (see the supplementary material[19] for more details). A KrF excimer laser (λ = 248 nm) with a fluency of ~2 J cm^{-2} and repetition rate 1 Hz was employed to ablate material from a stoichiometric $La_{0.7}Sr_{0.3}MnO_3$ target. The deposition took place in 0.35 milibars of oxygen at 540 °C, with a substrate-to-target separation of 45 mm, consistent with growth conditions for thermalized adatoms.[18] The growth was monitored with reflection high energy electron diffraction (RHEED). After deposition, the films were cooled to room temperature in 100 milibars of oxygen. The crystalline structure was examined using a four-circle, high-resolution x-ray diffractometer. The films were epitaxial, with an in-plane d-spacing along [1-10] of 2.25 Å consistent with the substrate value (see the supplementary material[19]). No structural domains were found, and the symmetry was confirmed to be hexagonal. The step-edges were observed to align with one of the in-plane $\langle 11\text{-}2 \rangle$ directions for all films. The thickness of the samples was determined correlating RHEED oscillations during growth, cross-section tunneling electron microscopy, and size effects in XRD.

Macroscopic magnetic data were taken with a vibrating sample magnetometer (VSM). The saturation magnetization was found to be 2.5 μ_B per Mn atom and the coercive field was 1.1 Oe at
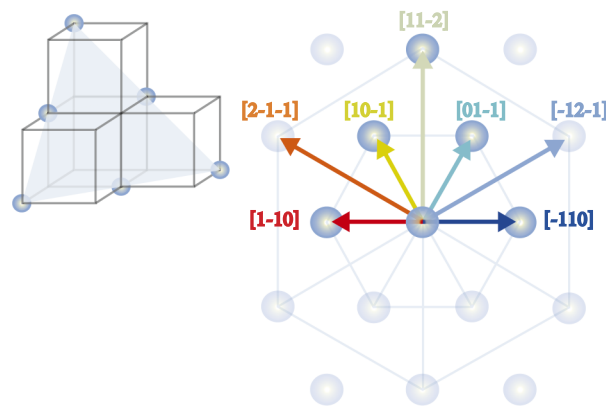

FIG. 1. (a) Schematic of the atomic configuration of a (111)-oriented surface in a cubic perovskite, with indications of the in-plane low-index directions, i.e., $\langle 1\text{-}10 \rangle$ and $\langle 11\text{-}2 \rangle$.

150 K, while the Curie temperature was determined at 335 K. At 50 K, the coercive field increases to 10 Oe (see supplementary material[19]). The observed saturation magnetizations and Curie temperatures are less than those reported for (001)-oriented films of the thicknesses investigated in the present study. However, the coercive fields obtained are typically an order of magnitude lower than those published for (001)-oriented films,[13,20] which indicates that domain walls move freely without significant pinning.[13] No apparent in-plane directional variation in coercive field or magnetization was found (see the supplementary material[19]), suggesting a macroscopically isotropic in-plane anisotropy of the samples, in accordance with bulk data.[11,14]

In order to probe the microscopic response of individual domains during magnetization reversal, the films were imaged by x-ray photoemission electron microscopy (PEEM) combined with x-ray magnetic circular dichroism (XMCD) at the Surface/Interface: Microscopy (SIM) beam line at the Swiss Light Source.[21,22] XMCD provides information on the projection of the magnetization vector along the helicity vector of circularly polarized x-rays. Thus, it is possible to obtain the components of the magnetization vector by rotating the sample relative to the incident beam of x-rays. XMCD was measured at the Mn L_3 absorption edge, with a photon energy of 642.7 eV, at room temperature. The inclination with film surface of the incident x-rays was 16°. The measured intensity of the magnetic circular dichroism is given by $I_{XMCD} \propto \langle M \rangle_T \cos \theta$, where θ is the angle between the x-ray helicity vector and the magnetization direction, and $\langle M \rangle_T$ is the temperature dependent average of the magnetic moment. PEEM allows for spatial mapping of x-ray absorption at the lateral length scale of single magnetic domains. Thus, when combined with XMCD, the magnetization orientation of individual magnetic domains can be determined.[21] The XMCD-PEEM images presented are divided images recorded with opposite polarization chirality (right/left circular).

Figure 2(a) shows an XMCD-PEEM image of the magnetic domain structure typically observed. We observe three different domains, where all three extend up to 125 μm in the vertical direction of the image. This is large compared to magnetic domains found in (001)-oriented films, in which reported magnetic domain sizes are typically between 1 and 25 μm,[9,23] and consistent
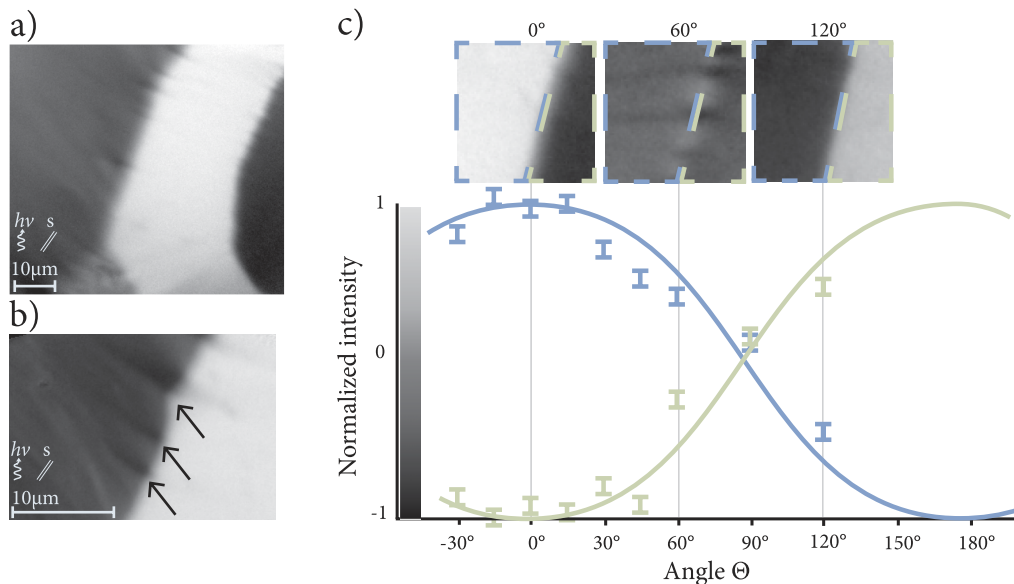
FIG. 2. XMCD-PEEM images and analysis of the domain structure, recorded at room temperature. The curved arrow denotes the incoming light (hv); the two parallel stripes indicate the direction of the step-edges (s). (a) XMCD-PEEM image of typical domain structure observed: uniform domains, which extend up to 30×125 μm. (b) XMCD-PEEM image across a domain wall. The arrows point where the domain wall resembles a cross-tie. (c) A plot of the average contrast in two different domains under azimuthal rotation, where the in-plane angle of the crystallographic $\langle 11$-$2 \rangle$ axes is defined to be $\theta = 0°$, 60°, 120°, with the [11-2] direction as 0°. The solid line represents a fit to a cosine function. The insets show XMCD-PEEM images for 0°, 60°, and 120°. The vertical scale bar denotes the relationship between grey-scale and normalized intensity for PEEM images in both (a), (b) and (c).

with the low degree of pinning discussed from magnetometry.[13] The domains are uniform with no indication of stripe-shaped domains following the step-edges, or rippling, as previously reported for (001)-oriented films.[9,23] In Figure 2(b), the domain wall region is shown, revealing a local domain wall structure, which resembles a cross-tie wall.[24] The ferromagnetic origin of the observed domain structure was confirmed by heating the sample above the Curie temperature, upon which the domain contrast disappeared.

The respective magnetization directions of two adjacent domains were found by azimuthal rotation of the sample, as shown in Figure 2(c). This plot presents the measured XMCD contrast as a function of angle, where the in-plane angle of the crystallographic $\langle 11\text{-}2 \rangle$ axes is defined to be $\theta = 0°, 60°, 120°$. The insets show images of the two domains at $\theta = 0°, 60°, 120°$. The contrast of an imaged domain is measured using the maximum of an intensity histogram normalized by area, and the plotted error bars in Figure 2 represent the full width at half maximum of these histograms. The measured contrast fits well with the expected azimuthal cosine dependence as described above. The maximum/minimum contrasts represent the directions for which the incoming x-rays are parallel to the magnetization vector. The magnetization vector of these adjacent domains is oppositely oriented, both being parallel to one of the in-plane $\langle 11\text{-}2 \rangle$ directions, which is also parallel to the direction of the step-edges. We note that if the global magnetic easy axis is along this in-plane $\langle 11\text{-}2 \rangle$ direction, it coincides with the step-edge direction, as reported for (001)-oriented samples.[23]

In order to elucidate a possible relationship between the in-plane crystallographic structure and the magnetic anisotropy of (111)-oriented $La_{0.7}Sr_{0.3}MnO_3$, the magnetic domain reversal process was investigated by applying magnetic field pulses of increasing magnitude and imaging the resulting remanent domain structure after each pulse. The field pulses were of 1 s duration with an increment of maximum 1 Oe per step. In Figure 3, we present images after different fields have been applied utilizing three representations for the magnetic domain contrast, schematically drawn in 3(a). Figure 3(b) depicts the XPEEM image on a normalized grey scale, as seen in 3(a). Figure 3(c) depicts the XPEEM image with colored areas where the magnetization directions correspond to the low-index angles as shown by the arrows in 3(a). Figure 3(d) is stylized images to highlight the relationship between magnetization direction (drawn as arrows) and domain wall structure. The reversal series is shown with the three representations for the magnetic contrast in 3(e)–3(g).

The initial magnetization (first panel in 3(e)–3(g)) was set by applying a large magnetic field pulse along one of the in-plane $\langle 1\text{-}10 \rangle$ directions, taken as the [1-10] direction. The reversal series shows selected images in which significant changes in the domain structure were found. Several trends can be identified: primarily, the data show that the initial direction of magnetization reverses (from bright to dark in 3(e)) by intermediate steps of different magnetization directions (different grey colors). During this magnetization reversal, new stripe-shaped domains emerge, and the orientation of these stripes rotates with increasing switching field. When the magnetization direction is fully reversed (last panel), the stripe domains are no longer visible. Hence, magnetization reversal occurs locally through domain formation and propagation rather than by rotation of the magnetic moments.

From Figure 3(f), it is clear that the magnetization direction of the various domains forming during switching corresponds to low-index in-plane crystal axes. As the amplitude of the field pulses is increased, new domains emerge with the magnetization direction shifted by 30° until a full 180° reversal is completed. In the first panel, the domain shown is fully magnetized by the external field. The direction of the magnetization is denoted with red arrows in Figure 3(g). In the second panel, a small pulse was applied, displaying formation of stripe-domains with a magnetization vector 30° off the initial direction of magnetization. In the third panel, these domains have grown at an expense of the initial domain, and a wide stripe with new domains has formed, where the magnetization is rotated 60° with respect to the initial magnetization. As the predominant magnetization direction approaches 90° with respect to the applied field, the domain structure is more complex, and is made up by smaller domains with different directions of their magnetization vector. Between applied fields of 13-20 Oe (three middle panels), there are also domains magnetized at angles of 75° and 105°, i.e., not aligned with the in-plane low-index axes. However, as the amplitude of the field pulses is increased, the majority of the domains magnetize along the $\langle 1\text{-}10 \rangle$ and $\langle 11\text{-}2 \rangle$ in-plane directions before the observed region is completely magnetized parallel to the applied field (the last
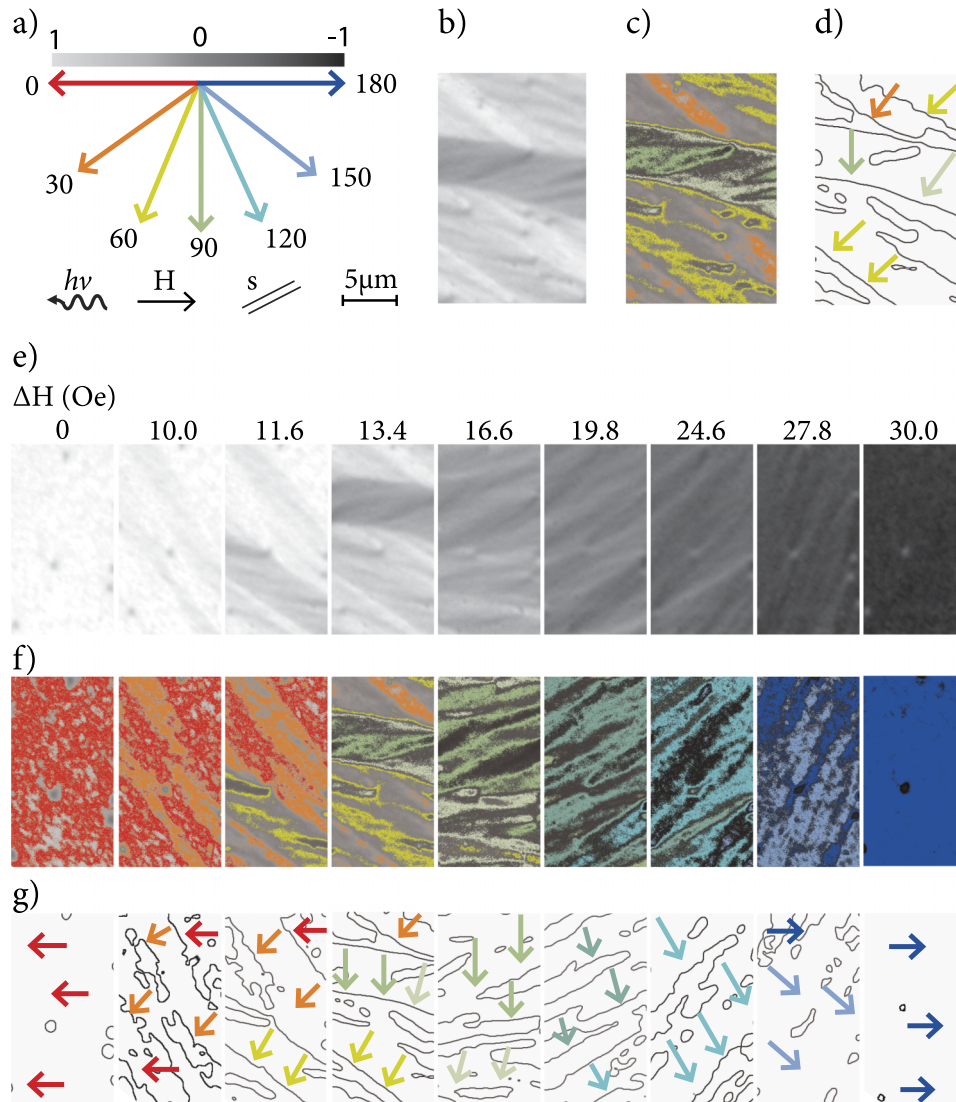
FIG. 3. XMCD-PEEM images of the remanent domain structure during magnetization reversal, taken at room temperature and utilizing three different representations for magnetic domain contrast. (a) Schematic of the different directions and scalebars used in the figure. The direction of the incoming light is drawn as a curved arrow (*hv*), the external field as a straight arrow (H), and the step edges as two straight lines (s). The size scale is applicable to all of the images in the figure. The divided XMCD images of opposite polarization (right/left circular) are shown in a normalized grey scale, where $1(-1)$ represents a magnetization direction parallel(antiparallel) to the incoming light. The colored arrows represent discrete magnetization directions that coincide with low-index crystal directions as shown in Figure 1, where red = 0° ([1-10]), orange = 30° ([2-1-1]), yellow = 60° ([10-1]), green = 90° ([11-2]), turquoise = 120° ([01-1]), light blue = 150° ([-12-1]), and blue = 180° ([-110]). (b) XMCD image of the domain structure using the grey scale contrast. (c) Same image as in (b) with regions where the magnetization direction coincides with the low-index crystal directions are colored according to the color scheme in (a). The colored areas are within the full width at half maximum of a typical histogram of one domain for the calculated intensities for the in-plane angles. (d) A stylized image of the image in (b) to highlight domain walls. The arrows represent the magnetization direction in each respective domain, following the color scheme in (a). (e) A series of XMCD images of the same region of the sample during magnetization reversal in the grey scale. The magnetization was reversed by an increasing positive field pulse after saturation in negative field. The magnitude of the pulse is indicated above each panel, with an errorbar of ±5 Oe for the base line. (f) The series of images in (e) with colored regions using the color scheme in (a). (g) The series of images in (e) stylized to highlight domain walls and with arrows representing the magnetization direction as in (a).

panel). On a local scale, the magnetization directions are clearly coupled to the crystal symmetry, with the magnetization preferentially aligned with the in-plane symmetry axes of ⟨1-10⟩ and ⟨11-2⟩.

The domain structure emerging during magnetization reversal consists of new stripe-shaped domains that rotate upon increasing the external field. In Figure 3(g), domain boundaries are highlighted to illustrate this effect. The direction of the stripes coincides with the in-plane low-index crystalline directions, with new stripes nucleating at 30° to the domains formed upon the previous field pulses. The magnetization vector of these stripe domains is typically oriented perpendicular to the direction of the stripe domain walls.

For thin films of (111)-oriented $La_{0.7}Sr_{0.3}MnO_3$, as was also reported for single crystals of $La_{0.7}Sr_{0.3}MnO_3$, no well-defined macroscopic easy and hard axes are observed. However, our XMCD-PEEM data show that the magnetization direction for individual domains is coupled to the hexagonal crystal symmetry of the (111) facet. When applying a macroscopic magnetic field along different crystalline directions, domains form locally with their magnetization along one of the low-index axes. We note that the XMCD-PEEM experiments image the remanent domain structure following a field pulse and, therefore, cannot be directly compared with the macroscopic hysteresis data. However, the measured averaged magnetization can be taken as the vector sum of the magnetization of all domains. Hence, as new domains appear at the expense of previous domains during the switching process, the resulting magnetization vector will rotate uniformly. We note that a hexagonal symmetry in Fe (111) epitaxial films displays a lower magnetic anisotropy as compared to cubic Fe epitaxial films,[25] supporting a weaker magnetic anisotropy in $La_{0.7}Sr_{0.3}MnO_3$ (111) with the 6-fold symmetry as compared to (001)-oriented samples with biaxial symmetry.

In summary, our data expand the overall picture of magnetocrystalline anisotropy in $La_{0.7}Sr_{0.3}MnO_3$; (001)-oriented films have biaxial anisotropy along the ⟨110⟩ axes, which coincides with the (001) projection of the (111) in-plane ⟨1-10⟩ directions. In (110)-oriented thin films, the anisotropy is uniaxial giving an easy axis along ⟨001⟩ directions originating from magnetostriction, but with an out-of-plane component, which fits well with a magnetocrystalline force pulling the easy axis towards the (111)-plane.[17] Although single crystals are reported to have a magnetic easy plane, the (111) plane, this study reveals a 6-fold anisotropy along the ⟨1-10⟩ and ⟨11-2⟩ in-plane directions. This local coupling between magnetization and symmetry affects the magnetization reversal, which proceeds by stepwise nucleation of stripe-domains with magnetization along the different easy axes. Hence, it is possible to control the magnetic anisotropy using different crystallographic symmetries, thereby changing the domain structure and the switching characteristics. Thus, crystal orientation may serve to tailor the switching mechanism in devices.

[1] G. H. Jonker and J. H. Van santen, Physica **16**(3), 337 (1950).

[2] J.-H. Park, E. Vescovo, H.-J. Kim, C. Kwon, R. Ramesh, and T. Venkatesan, Nature **392**(6678), 794 (1998).

[3] A.-M. Haghiri-Gosnet and J.-P. Renard, J. Phys. D: Appl. Phys. **36**, R127 (2003).

[4] E. Dagotto, T. Hotta, and A. Moreo, Phys. Rep. **344**(1-3), 1 (2001).

[5] M. Bowen, M. Bibes, A. Barthélémy, J.-P. Contour, A. Anane, Y. Lemaître, and A. Fert, Appl. Phys. Lett. **82**(2), 233 (2003).

[6] M. Cesaria, A. P. Caricato, G. Maruccio, and M. Martino, J. Phys.: Conf. Ser. **292**(1), 012003 (2011).

[7] S. Majumdar and S. van Dijken, J. Phys. D: Appl. Phys. **47**(3), 15 (2014).

[8] A. Khapikov, L. Uspenskaya, I. Bdikin, Y. Mukovskii, S. Karabashev, D. Shulyaev, and A. Arsenov, Appl. Phys. Lett. **77**(15), 2376 (2000).

[9] M. Ziese, Phys. Status Solidi B **243**(6), 1383 (2006).

[10] D. Ecija, E. Jiménez, N. Mikuszeit, N. Sacristán, J. Camarero, J. M. Gallego, J. Vogel, and R. Miranda, Phys. Rev. B **77**(2), 024426 (2008).

[11] M. Konoto, T. Kohashi, K. Koike, T. Arima, Y. Kaneko, Y. Tomioka, and Y. Tokura, Appl. Phys. Lett. **84**(13), 2361 (2004).

[12] Y. Suzuki, H. Y. Hwang, S.-W. Cheong, and R. B. van Dover, Appl. Phys. Lett. **71**(1), 140 (1997).

[13] L. M. Berndt, V. Balbarin, and Y. Suzuki, Appl. Phys. Lett. **77**(18), 2903 (2000).

[14] H. Boschker, J. Kautz, E. P. Houwman, G. Koster, D. H. A. Blank, and G. Rijnders, J. Appl. Phys. **108**(10), 103906 (2010).

[15] M. Gibert, P. Zubko, R. Scherwitzl, J. Íñiguez, and J.-M. Triscone, Nat. Mater. **11**(3), 195 (2012).

[16] J. Chakhalian, A. J. Millis, and J. Rondinelli, Nat. Mater. **11**(2), 92 (2012).

[17] R. V. Chopdekar, E. Arenholz, and Y. Suzuki, Phys. Rev. B **79**(10), 104417 (2009).

[18] I. Hallsteinsen, J. E. Boschker, M. Nord, S. Lee, M. Rzchowski, P. E. Vullum, J. K. Grepstad, R. Holmestad, C. B. Eom, and T. Tybell, J. Appl. Phys. **113**(18), 183512 (2013).

[19] See supplementary material at http://dx.doi.org/10.1063/1.4907877 for details on macroscopic, magnetic, and structural characterizations.

[20] P. Perna, C. Rodrigo, E. Jiménez, F. J. Teran, N. Mikuszeit, L. Méchin, J. Camarero, and R. Miranda, J. Appl. Phys. **110**(1), 013919 (2011).

[21] M. R. Scheinfein, S. Anders, T. Stammler, H. A. Padmore, and J. Stöhr, Surf. Rev. Lett. **05**(06), 1297 (1998).

[22] L. Le Guyader, A. Kleibert, A. Fraile Rodríguez, S. El Moussaoui, A. Balan, M. Buzzi, J. Raabe, and F. Nolting, J. Electron Spectrosc. Relat. Phenom. **185**(10), 371 (2012).

[23] T. Taniuchi, H. Kumigashira, M. Oshima, T. Wakita, T. Yokoya, M. Kubota, K. Ono, H. Akinaga, M. Lippmaa, M. Kawasaki, and H. Koinuma, Appl. Phys. Lett. **89**(11), 112505 (2006).

[24] S. Middelhoek, J. Appl. Phys. **34**(4), 1054 (1963).

[25] S. M. Rezende, J. A. S. Moura, F. M. de Aguiar, and W. H. Schreiner, Phys. Rev. B **49**(21), 15105 (1994).